RESOURCE GEOLOGY

doi: 10.1111/j.1751-3928.2011.00177.x *Resource Geology* Vol. 62, No. 1: 4–18

Thematic Article

Highly Oxidized Magma and Fluid Evolution of Miocene Qulong Giant Porphyry Cu-Mo Deposit, Southern Tibet, China

Bo XIAO,[1,2] Kezhang QIN,[1] Guangming LI,[1] Jinxiang LI,[1] Daixiang XIA,[3] Lei CHEN[1,2] and Junxing ZHAO[1,2]

[1]*Key Laboratory of Mineral Resources, Institute of Geology and Geophysics, Chinese Academy of Sciences,* [2]*Graduate University of Chinese Academy of Sciences, Beijing and* [3]*Tibet Julong Copper Co., Ltd, Lhasa, China*

Abstract

The Miocene Qulong porphyry Cu-Mo deposit, which is located at the Gangdese orogenic belt of Southern Tibet, is the largest porphyry-type deposit in China, with confirmed Cu ~10 Mt and Mo ~0.5 Mt. It is spatially and temporally associated with multiphase granitic intrusions, which is accompanied by large-scale hydrothermal alteration and mineralization zones, including abundant hydrothermal anhydrite. In addition to hydrothermal anhydrite, magmatic anhydrite is present as inclusions in plagioclase, interstitial minerals between plagioclase and quartz, and phenocrysts in unaltered granodiorite porphyry, usually in association with clusters of sulfur-rich apatite in the Qulong deposit. These observations indicate that the Qulong magma-hydrothermal system was highly oxidized and sulfur-rich. Three main types of fluid inclusions are observed in the quartz phenocrysts and veins in the porphyry: (i) liquid-rich; (ii) polyphase high-salinity; and (iii) vapor-rich inclusions. Homogenization temperatures and salinities of all type inclusions decrease from the quartz phenocrysts in the porphyry to hydrothermal veins (A, B, D veins). Microthermometric study suggests copper-bearing sulfides precipitated at about 320–400°C in A and B veins. Fluid boiling is assumed for the early stage of mineralization, and these fluids may have been trapped at about 35–60 Mpa at 460–510°C and 28–42 Mpa at 400–450°C, corresponding to trapping depths of 1.4–2.4 km and 1.1–1.7 km, respectively.

Keywords: fluid inclusion, Gangdese, highly oxidized, magmatic anhydrite, Qulong porphyry Cu–Mo deposit, Sulfur-rich magma.

1. Introduction

Magmas associated with porphyry Cu mineralization are oxidized and contain sulfur as sulfates, such as SO_4^{2-} (Ishihara, 1977; Burnham & Ohmoto, 1980; Blevin & Chappell, 1992; Keith & Swan, 1995). Calc-alkaline volcanic rocks, particularly those rich in hornblende or biotite, appear to have crystallized at oxygen fugacity (fO_2) high enough to stabilize anhydrite (Imai, 2002). Primary magmatic anhydrite ($CaSO_4$) which precipitates directly from silicate melts is rare in volcanic rocks and has been reported in only a few locations, such as El Chichón in Mexico (Luhr *et al*., 1984) and Mount Pinatubo in the Philippines (Bernard *et al*., 1991).

The Qulong porphyry Cu–Mo deposit is located at the center part of the newly discovered Gangdese metallogenic belt in southern Tibet. The deposit was first explored in its northern part, and the Tibet Julong

Received 6 June 2010. Accepted for publication 25 October 2011.
Corresponding author: K. QIN, Key Laboratory of Mineral Resources, Institute of Geology and Geophysics, Chinese Academy of Sciences, Beijing 100029, China. Email: kzq@mail.iggcas.ac.cn

Copper Co., Ltd. (2008) reported resources of 7.19 Mt Cu and 0.35 Mt Mo. During 2008 and 2009, the company prospected in the southern part and gained additional resources of about 2.87 Mt Cu and 0.15 Mt Mo. The Qulong deposit is now the largest porphyry Cu deposit in China, with at least ~10.6 Mt Cu, average 0.5% and ~0.5 Mt Mo, average 0.03%. Compared with other Cenozoic porphyry deposits in the Gangdese metallogenic belt, the Qulong deposit is characterized by larger-scale hydrothermal alteration and mineralization zones, and abundance in hydrothermal veins and anhydrite. Hydrothermal anhydrite is one of the most abundant hydrothermal minerals in the deposit, and magmatic anhydrite occurs in some unaltered intrusive rocks. The occurrence of magmatic and hydrothermal anhydrite indicates that the magmatic-hydrothermal system at Qulong is highly oxidized and sulfur-rich.

In order to reveal the nature of the highly oxidized, S-rich ore-forming magma-hydrothermal system, this paper describes geological and mineralogical features of the Qulong deposit, as well as the result of fluid inclusion microthermometry.

2. Geology of the deposit

In southern Tibet, the Lhasa terrane is mainly composed of the Gangdese orogenic belt, which resulted from the northward subduction of the Neo-Tethyan oceanic lithosphere beneath Asia and subsequent India–Asia collision (Yin & Harrison, 2000; Aitchison *et al*., 2007). The Gangdese orogenic belt consists mainly of Late Paleocene–Early Eocene (60–40 Ma) Linzizong Formation volcanic rocks and Cretaceous-Tertiary (120–24 Ma) granite batholiths (Allègre *et al*., 1984; Coulon *et al*., 1986; Mo *et al*., 2007, 2008). According to Harrison *et al*. (1992), rapid uplift of southern Tibet took place at about 20 Ma, and then the N-S-trending rift system developed across the Gangdese belt (Coleman & Hodges, 1995; Harrison *et al*., 1995; Williams *et al*., 2001) due to a regional E-W extension (Williams *et al*., 2001). In the Indo-Asian collision, multiple metallogenic events occurred in the different tectonic settings: main-collisional convergent setting (~65–41 Ma), late-collisional transform setting (~40–26 Ma) and post-collisional crustal extension setting (~25–0 Ma) (Hou *et al*., 2006a, b, c, 2009).

The Cenozoic post-collisional Gangdese metallogenic belt is newly identified (Qu *et al*., 2004; Hou *et al*., 2006a, b, c, 2009; Li *et al*., 2006a, 2007a; Qin *et al*., 2008) along the Gangdese orogenic belt, which contains more than 10 Cenozoic porphyry deposits. Qin *et al*. (2005) emphasized those Miocene porphyry Cu deposits formed in a transitional tectonic setting from compression to extension. The Qulong porphyry Cu–Mo deposit is the largest among them, which is located in the southern part of Gangdese orogenic belt (latitude 29°36′–29°40′ N, longitude 91°33′–91°37′ E), about 50 km east of Lhasa city, the capital of Tibet Autonomous Region and 45 km north of the Yarlung-Tsangpo River (the Yarlung-Tsangpo suture zone) (Fig. 1).

The Qulong deposit is intimately associated with the Miocene multiphase granitic intrusions, with large-scale (4×8 km^2) hydrothermal alteration and mineralization zones (with a vertical extent more than 1350 m), including abundant hydrothermal veins and anhydrite. The multiphase granitic intrusions range from 18 Ma to 14 Ma (Rui *et al*., 2003; Wang *et al*., 2006; Yang *et al*., 2009) and molybdenite Re-Os age in the deposit is 16.0 ± 0.3 Ma (Rui *et al*., 2003). These ages correspond to the timing of the post-collisonal orogenic setting. A sequence of Miocene intrusions observed is: granodiorite, biotite monzogranite, monzogranitic porphyry, granodiorite porphyry and diorite porphyrite. These rocks intruded into the volcanic rocks of the Jurassic Yeba Formation (Dong *et al*., 2006; Geng *et al*., 2006) (Fig. 1).

Among the intrusive rocks, the granodiorite (Figs 1, 2b) strikes approximately east–west in the Yeba Formation. It is the earliest intrusion and with an outcrop area of >5 km^2. It consists of medium- to coarse-grained plagioclase (40–45 volume %), K-feldspar (15–20 vol. %), quartz (10–15 vol. %) and minor hornblende (10–15 vol. %) and biotite (10 vol. %). Accessory minerals are zircon, apatite, magnetite and sphene.

The biotite monzogranite (Figs 1, 2c) is outcropped in an area of 4 km^2 in the center part of the ore district. This monzogranite is composed of medium- to coarse-grained plagioclase (35–40 vol. %), K-feldspar (20–25vol. %), anhedral quartz (20–25 vol. %) and minor biotite (10–15 vol. %) and lacks in hornblende. Accessory minerals are zircon, apatite, magnetite and rutile. The monzogranite contains more biotites and quartz than the granodiorite.

The light gray monozogranite porphyry (Figs 1, 2d) is a small dike, intruded into biotite monzogranite, with an outcrop area of ~0.5 km^2 in the eastern part of the monzogranitic porphyry (Fig. 1). The monozogranite porphyry is of granitic composition and typical porphyritic texture, with a mineral assemblage of plagioclase (15–20 vol. %), K-feldspar (10 vol. %),

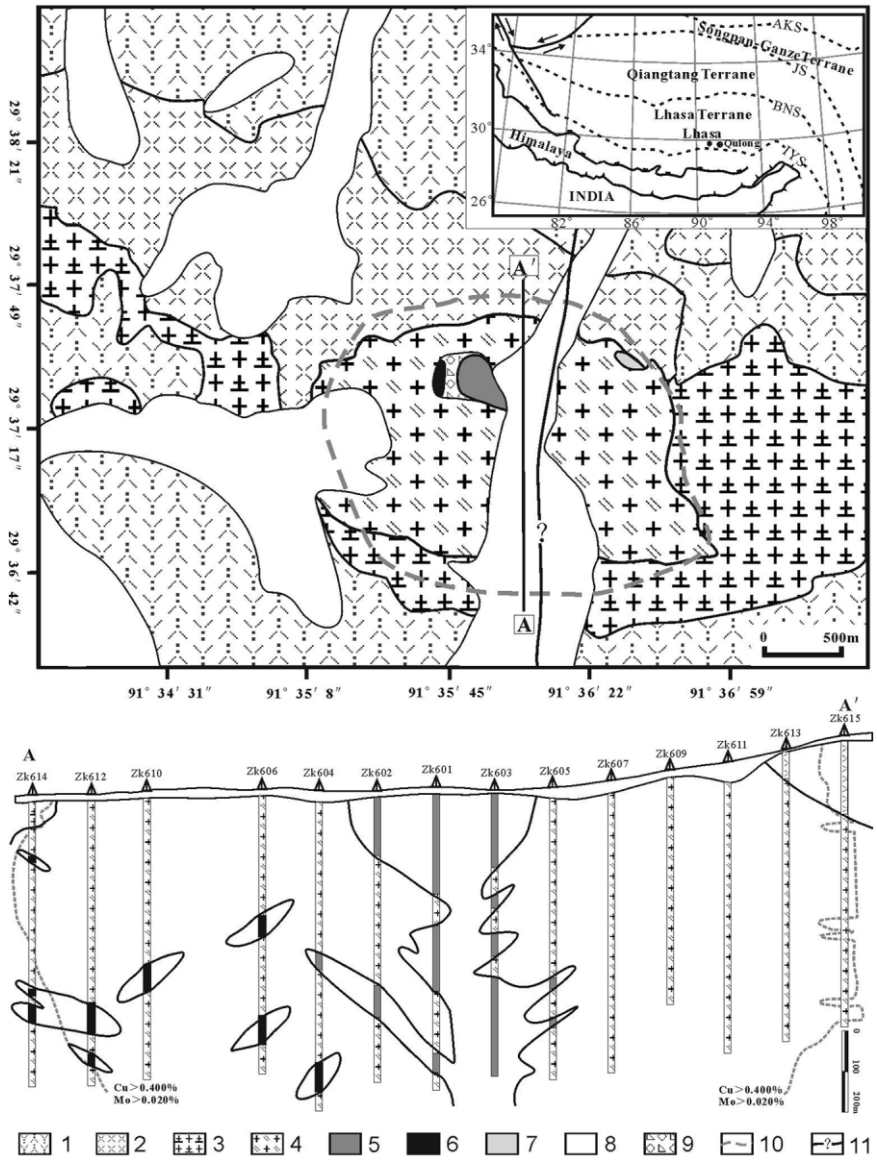

Fig. 1 Geology sketch map of the Qulong porphyry Cu–Mo deposit after Tibet Julong Copper Co., Ltd. (2008) and Xiao *et al*. (2009). 1: Tuff of the Jurassic Yeba Fomation; 2: rhyolite of the Yeba Formation; 3: Miocene granodiorite; 4: Miocene biotite monozogranite; 5: Miocene monozogranite porphyry; 6: Miocence granodiorite porphyry; 7: Miocene diorite porphyrite; 8: Quaternary; 9: breccia; 10: orebody boundary; 11: unidentified fault.

quartz (10–15 vol. %) phenocrysts in an aphanitic groundmass of quartz, plagioclase and K-feldspar. Biotite phenocrysts are present (3–5 vol. %). Apatite and zircon are accessory minerals. Anhydrite as mineral inclusions is occasionally observed in feldspar phenocrysts.

The gray granodiorite porphyry (Figs 1, 2e) is small dike bodies intruding in the northwest part of biotite monozogranite with an outcrop area of 0.4 km^2. It occurs as thin dikes ranging from 0.5 to 80 m in many drill cores. The mineral assemblage of this rock is plagioclase (20–25 vol. %), K-feldspar (5–10 vol. %), quartz (5–10 vol. %) and biotite (5–10 vol. %) phenocrysts in an aphanitic groundmass of quartz, plagioclase, K-feldspar and biotite. Anhydrite, apatite, zircon and magnetite are accessory minerals. Anhydrite occurs as microphenocryts and phenocryts, usually coexisting with apatite or intergrows with plagioclase.

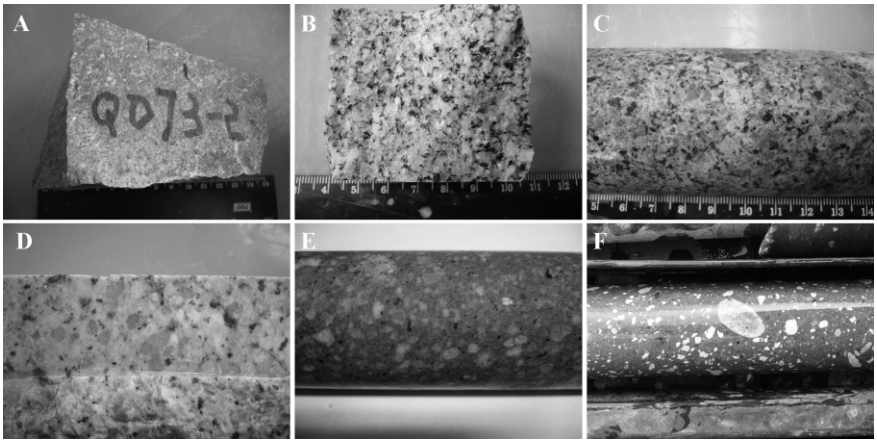

Fig. 2 Photographs of the rocks from the Qulong porphyry Cu–Mo deposit. a: Tuff of the Yeba Formation, b: Miocene granodiorite, c: Miocene biotite monozogranite, d: Miocene monozogranite porphyry, e: Miocene granodiorite porphyry, f: Miocene diorite porphyrite.

The diorite porphyrite (Figs 1, 2f) occurs as a stock intruded into biotite monzogranite in the central part of the ore district. The minerals of this rock is rounded K-feldspar (10 vol. %), plagioclase (5 vol. %), hornblende (10–15 vol. %) and quartz (3 vol. %) phenocrysts in a finer-grained groundmass of hornblende and plagioclase. Apatite, zircon and sphene are accessory minerals. The rounded quartz and K-feldspar phenocrysts mainly range from 2 to ≥20 mm and with a distinct corroded boundary which indicates those phenocrystys are xenocrysts.

Except the diorite porphyrite, the Miocene intrusions are characterized by adakite-like geochemical affinities, with >60 wt% SiO_2, >14 wt% Al_2O_3, usually <2 wt% MgO (400–1300 ppm) Sr (5–9 ppm) Y, and Sr/Y (60–160) (Defant & Drummond, 1990; Yang *et al*., 2009).

The granodiorite underwent alteration manifested by minor secondary biotite and kaolinite replacing biotite, hornblende and plagioclase, minor chlorite replacing biotite, and along with very small grains of epidote. Chlorite completely or partially replaced hornblende and biotite along mineral rims and cleavage planes. The biotite monzogranite is characterized by extensive weak argillic and potassic alteration, and locally intermediate argillic alteration in shallow depth and K-feldspar alteration in deep levels, respectively; secondary biotite + anhydrite alteration is the most pervasive alteration. The biotite monzogranite is associated with abundant disseminated and stockwork chalcopyrite, molybdenite and pyrite mineralization. The monozogranite porphyry underwent argillic alteration and potassic alteration, including local intensive K-feldspar alteration. The granodiorite porphyry underwent weak argillic alteration with rare disseminated pyrite + chalcopyrite or pyrite + chalcopyrite thin veins. The porphyrite is unaltered and barren. Hydrothermal breccia is distributed around the granodiorite porphyries.

The hydrothermal alteration of the deposit is centered on the monozogranite porphyry and changes from potassic alteration to phyllic, argillic and propylitic alteration upwards. Hydrothermal anhydrite, which crystallized together with quartz, biotite, K-feldspar, sericite and sulfides, is ubiquitous in the potassic and phyllic zones. The single orebody with networks of veinlets, veins and disseminated copper mineralization, is hosted in biotite monzogranite, monzogranitic porphyry and granodiorite porphyry, but rare in the granodiorite and Jurassic rocks. The orebody is rare in supergene enrichment, which occurs locally on the surface. Sulfides include abundant pyrite, chalcopyrite, molybdenite, a few bornite, chalcocite, and trace sphalerite and galena. Main gangue minerals are quartz, anhydrite, biotite, sericite, K-feldspar, plagioclase and clay minerals. Molybdenite is mainly hosted in quartz + molybdenite veins, which usually crosscut the early chalcopyrite–pyrite bearing veins; disseminated molybednite is rare.

The hydrothermal veins at Qulong are classified into five types based on the mineral assemblages and crosscutting relations (Table 1). These are named as A, EB, B, C and D veins on the basis of the classification by Gustafson and Hunt (1975) and Dilles & Einaudi (1992) (Fig. 3) The characters of the vein system are summarized in Table 1.

Table 1 Characters of vein system of the Qulong porphyry Cu–Mo deposit

	Typical veins	Morphology	Ore minerals	Occurrence	Alteration halo
A vein	Qz, Bi ± Qz ± Kf, Kf-Bi ± An, Qz-Kf ± Cpy ± Py ± Bn, Qz-An, Mt-Qz-Py-Cpy ± An	Commonly irregular, discontinuous, 0.1–10 mm	Cpy, Py, Bn, locally Mt; trace Mo	Abundant in monozogranite porphyry, biotite monozogranite; rarely in granodiorite	Halos of Kf, Bi and trace An
EB vein	Qz-Bi, Qz ± An ± Chl-Mt-Cpy-Py, Bi-Qz-Py-Cpy-Mo ± Bn ± Mt,	Irregular, continuous, 0.5–5 mm	Trace Mt, Cpy, Py, Mo, Bn	Abundant in biotite monozogranite	Halos of Bi, trace Chl
B vein	Qz-Bi ± An ± Chl ± Py ± Cpy, Qz-An ± Cpy ± Py ± Mo, Qz-Mo ± An ± Py ± Cpy, Cpy-Py ± Qz ± An	Regular, continuous; rarely irregular 1- >30 mm	Abundant Cpy, Py, Mo; rare Bn	Abundant in monozogranite porphyry, biotite monozogranite; rarely in granodiorite porphyry	Halos of weakly Bi, Ser and argillic; locally advanced argillic alteration
C vein	Chl-Py-Cpy ± Mt	Regular, continuous, 2–5 mm	Trace Py, Cpy	Only rarely in biotite monozogranite	Halos of weakly Ser, Chl, Gp
D vein	Qz-Py-Ser ± Cpy ± Ser, Qz-Ser, Ep-Cpy-Py, Qz ± An-Sph-Gal	Regular, continuous, 1–15 mm	Abundant Py; trace Cpy, Mo, Gal, Sph	Abundant in Jurassic tuff, granodiorite; rarely in monozogranite porphyry, biotite monozogranite	Halos of Ser, argillic, Chl, weakly calcite and rare Gp

An, anhydrite; Bi, biotite; Bn, bornite; Chl, chlorite; Cpy, chalcopyrite; Ep, epidote; Gal, galena; Gp, gypsum; Kf, K-feldspar; Mo, molybdenite; Mt, magnetite; Py, pyrite; Qz, quartz; Ser, sericite; Sph, sphalerite.

3. Sample description

3.1 Anhydrite

All the analyzed samples in this study are collected from drill cores. The sample numbers present the drill hole and downhole depth respectively, for example sample QZK401-430 is from drill hole ZK401 at the downhole depth of 430 m. Samples QZK401-430 and QZK301-142 are hydrothermal anhydrite-bearing mineralized veins (>2 cm in width), with assemblages of anhydrite + quartz + chalcopyrite + pyrite ± molybdenite. Samples QZK812-472 and QZK812-473 are unaltered granodiorite porphyry.

There are two distinctive types of anhydrite. The first type is hydrothermal anhydrite, which is commonly associated with pyrite, chalcopyrite, molybdenite, magnetite, quartz, forming hydrothermal breccia matrixes (Fig. 4a) and mineralized veins (Fig. 4b). The color is mainly purple in breccia and early A, B veins, and appear colorless or sky-blue in D veins. In some A and B veins, anhydrite may account for 25 to >90 vol. % of the gangue minerals and closely adjacent the sulfides. In late D veins, anhydrite distinctly decreased in volume (<5–10 vol. %). Altered rocks commonly include 1–5 vol. % hydrothermal anhydrite.

The second type is magmatic in origin, and occurs as inclusions in plagioclase in granodiorite and monzogranitic porphyry, or as phenocrysts with plagioclase and quartz in granodiorite and biotite monzogranite (Fig. 4c, d). The anhydrite phenocrysts usually coexist with apatite in unaltered granodiorite porphyry (Fig. 4e). The anhydrite microphenocrysts with distinct corroded boundaries are observed (Fig. 4e, f).

3.2 Fluid inclusions

Fluid inclusions at Qulong deposit are classified into three main types which are divided into nine subtypes. These types include: type 1, liquid-rich inclusions; type 2, vapor-rich inclusions; and type 3, polyphase high-salinity inclusions, containing a halite daughter phase and other opaque and/or translucent minerals. The characters of all fluid inclusions are summarized in Table 2.

Type 1 inclusions are divided into two subtypes based on the presence of opaque phase or reddish rounded (hematite) or transparent unknown silicate minerals: 1a, containing only two phases (L+V); 1b, usually containing a third phase (L+V+Op/Hem ± M), present in A and B veins and quartz phenocrysts. They are commonly rounded or negative-crystal in shape,

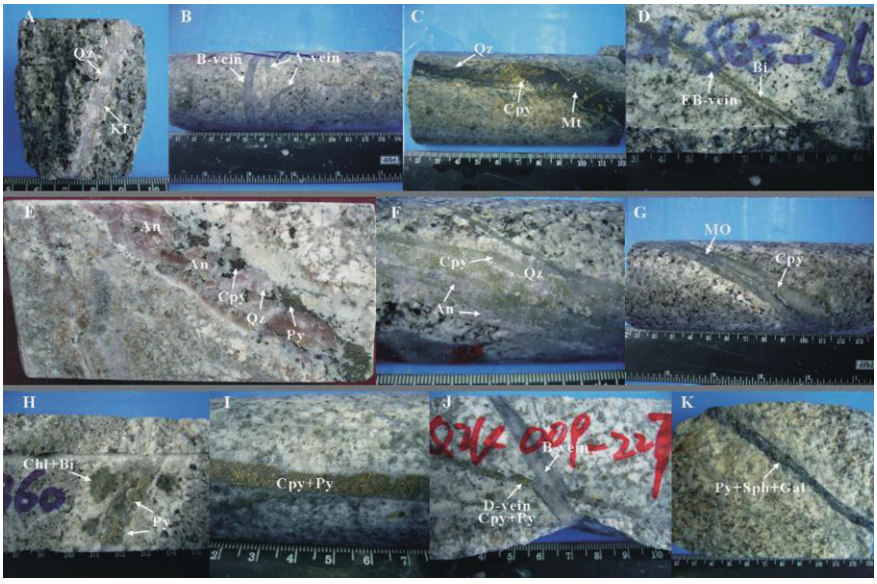

Fig. 3 Vein types in the Qulong porphyry Cu–Mo deposit. a: "A" vein with K-feldspar halo; b: "B" vein cuts irregular discontinuous "A" veins; c: "A" vein with Qz + Mt + Cpy ± Py; d: "EB" vein with biotite halo; e: "B" vein with sericite and argillic alteration halo; f: "B" vein with weakly feldspar-destructive halo; g: "B" vein with feldspar-destructive halo; h: "C" vein with sericite halo; i: regular "D" vein; j: "D" vein cuts "B" vein; k: "D" vein with feldspar-destructive halo. Qz: quartz, Kf: K-feldspar, An: anhydrite, Bi: biotite, Ep: epidote, Chl: chlorite, Py: pyrite, Cpy: chalcopyrite, Mo: molybdenite, Mt: magnetite, Gal: galena, Sph: sphalerite.

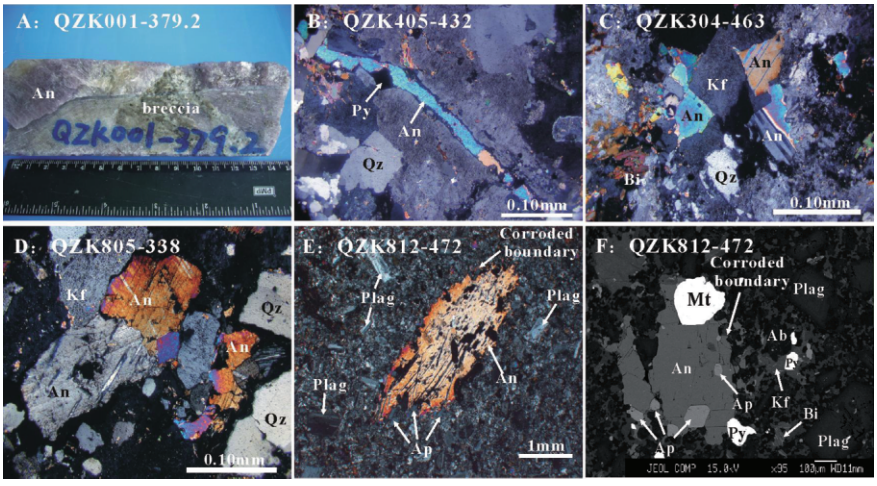

Fig. 4 Photographs, microphotographs and back-scattered electronic (BSE) images of anhydrite in the Qulong deposit. a: Photograph of hydrothermal breccia, with anhydrite matrix. b: Cross-polarized light photomicrograph of biotite monzogranite, with anhydrite + pyrite vein. c: Cross-polarized light photomicrograph of granodiorite, with interstitial anhydrite. d: Cross-polarized light photomicrograph of biotite monzogranite, with interstitial anhydrite. e: Cross-polarized light photomicrograph of granodiorite porphyry, with magmatic anhydrite phenocryst and clusters of apatite. f: BSE image of magmatic anhydrite microphenocryst and clusters of apatite, magnetite, pyrite. Ab: albite, An: anhydrite, Ap: apatite, Bi: biotite, Kf: K-feldspar, Mt: magnetite, Plag: plagioclase, Py: pyrite, Qz: quartz.

Table 2 Fluid inclusions in the Qulong porphyry Cu–Mo deposit

Type	Sub-type	Phases present at room temperature					Occurrence	Homogenization behavior
		Shape	Phase composition	Phase number	Daughter mineral	Size(μm)		
1	1a	Negative-crystal, regular, rounded forms	L+V	2	—	3–30	All samples	Vapor disappears
	1b	Negative-crystal, regular, rounded forms	L+V+Op/Hem ± M	3–4	Op, Hem, M	3–30	Abundant in A, B veins and quartz phenocrysts, rare in D veins	Vapor disappears
2	2a	Negative-crystal, regular, rounded forms	L+V	2	—	4–24	Abundant in A and quartz phenocrysts	Water disappear
	2b	Negative-crystal, regular, rounded forms	L+V+M/Op	3–4	M	2–20	Rare in A veins and quartz phenocysts	Water disappears
3	3a	Negative-crystal, rounded forms	L+V+H	3	H	4–26	All samples, except anhydrites	Halite/vapor disappear or both disappear at the same temperature
	3b	Negative-crystal, rounded forms	L+V+H+Op	4	H, Op	5–25	A, B veins and quartz phenocysts	Halite/vapor disappear, halite disappearance dominates
	3c	Negative-crystal, rounded forms	L+V+H+S ± Op ± Hem	4–6	H, S, Op, Hem	6–15	A, B veins and quartz matrixes of breccia	Halite disappears
	3d	Negative-crystal, rounded forms	L+V+H+Hem ± Op	4–5	H, Hem, Op	4–14	A, B veins and quartz matrixes of breccia	Halite disappears
	3e	Negative-crystal, rounded forms	L+V+H+M	4	H, M	4–12	Rare in A, B veins	Halite disappears

H, halite; Hem, hematite; M, transparent silicate mineral; Op, opaque mineral; S, sylvite.

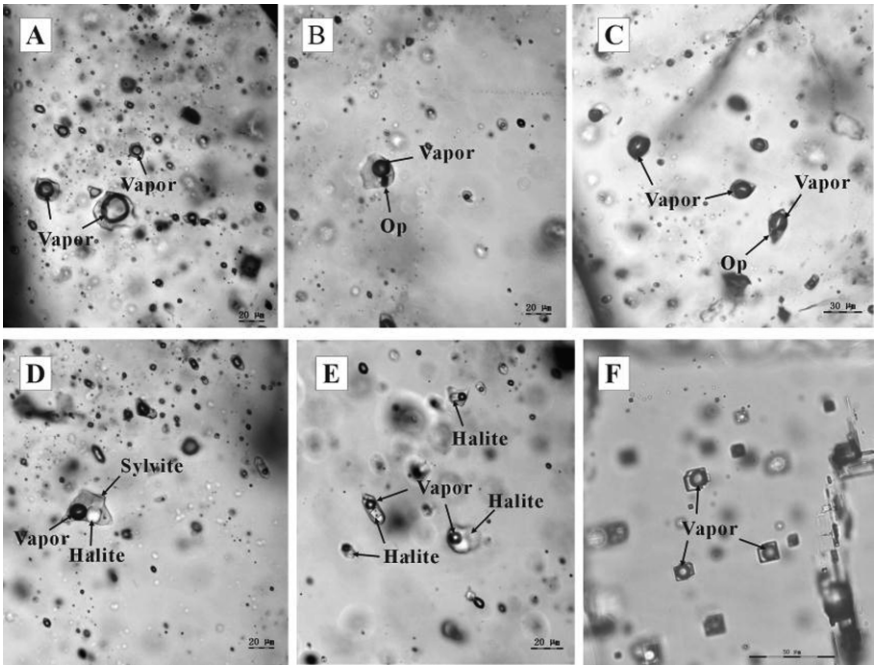

Fig. 5 Photomicrographs of fluid inclusions in the Qulong porphyry Cu–Mo deposit. a: Type 1, liquid-rich fluid inclusions, low salinity; b: type 1, liquid-rich fluid inclusions with Op; c: type 2, vapor-rich fluid inclusions with Op; d: type 3, polyphase fluid inclusions; e: type 3, polyphase fluid inclusions coexist with liquid-rich fluid inclusion; and f: type 1, liquid-rich fluid inclusions in anhydrite. Op: opaque mineral.

and range 3–30 μm (Fig. 5a, b). The vapor phase occupies between 5% and 35% volume. Final melting temperatures of ice ($T_{m.ice}$) were determined for calculating the salinities and all the inclusions were homogenized into liquid phase.

Type 2 inclusions range 4–24 μm in size and vary from negative-crystal shapes to irregular (Fig. 5c). The vapor phase occupies between >60% and 90% volume. They are divided into two subtypes based on the presence of opaque phase or transparent unknown silicate minerals: 2a, containing only two phases (L+V), present in A veins, matrix of breccia and quartz phenocrysts; 2b, usually containing a third phase (L+V+M/Op) rarely present in A veins and quartz phenocrysts. It is difficult to observe the process of freezing in these inclusions because of their dark cavity walls; only a few final melting temperatures of ice ($T_{m.ice}$) are measured. The limited fluid content makes exact determination of phase change difficult. A few vapor-rich inclusions, on heating, remained unchanged, until the temperature approached to approximately 20°C of the homogenization temperature, when the vapor phase then rapidly expanded to fill the inclusions; this indicates that these inclusions contain fluids with near-critical densities (Roedder, 1984).

Type 3 inclusions vary 4–26 μm in size and have negative-crystal shapes, or rounded forms (Fig. 5d, e). Vapor-phase contents vary 5–30 vol. %. Halite is identified based on its cubic crystal shape and absence of birefringence. Besides transparent daughter minerals, there are reddish rounded hematite (?) and variously rounded and/or triangular shape chalcopyrite (?) within the inclusions. Based on different phase compositions, these inclusions are divided into five subtypes: 3a contains three phases (L+V+H), homogenized by disappearance of vapor (T_f) or halite (T_{mNacl}) or vapor and halite disappearance approximately at the same temperature; 3b contains four phases (L+V+H+Op), homogenized by disappearance of vapor (T_f) or halite (T_{mNacl}), but halite disappearance dominates, presenting in A veins, B veins and quartz phenocrysts; 3c contains four to six phases (L+V+H+S ± Op ± Hem) with rounded shaped sylvite and/or opaque phase and/or reddish rounded (hematite?), homogenized by disappearance of halite (T_{mNacl}) in A veins, B veins and quartz phenocrysts; 3d contains four to five phases (L+V+H+Hem ± Op) with reddish rounded (hematite?) and/or opaque phases, homogenized by disappearance of halite (T_{mNacl}) in A veins, B veins and quartz phenocrysts; 3e contains four phases (L+V+H+M), with

Table 3 Electron probe microanalysis of anhydrite and apatite of the Qulong porphyry Cu–Mo deposit

	Magmatic anhydrite														
	QZK812-472								QZK812-473						
CaO	41.12	40.64	40.40	40.68	41.03	40.28	40.16	40.21	40.33	41.15	39.91	40.45	39.83	39.92	39.98
SO_3	59.60	58.71	59.62	59.80	58.91	59.67	58.91	59.56	59.13	58.14	58.43	59.04	58.62	58.09	58.44
P_2O_5	0.05	0.07	0.07	0.10	0.01	0.13	0.02	0.07	0.07	0.07	0.22	0.07	0.09	0.28	0.33
SiO_2	0.07	0.00	0.03	0.00	0.01	0.05	0.02	0.02	0.08	0.01	0.01	0.03	0.01	0.04	0.00
Ce_2O_3	0.04	0.04	0.00	0.11	0.00	0.10	0.00	0.05	0.00	0.05	0.15	0.15	0.13	0.10	0.21
MnO	0.00	0.00	0.00	0.01	0.00	0.01	0.00	0.00	0.00	0.00	0.00	0.00	0.01	0.01	0.00
BaO	0.00	0.00	0.02	0.02	0.01	0.00	0.00	0.00	0.06	0.00	0.08	0.00	0.00	0.00	0.00
SrO	0.08	0.02	0.02	0.01	0.04	0.03	0.06	0.00	0.11	0.00	0.00	0.07	0.02	0.00	0.00
Total	100.96	99.48	100.16	100.73	100.01	100.27	99.17	99.91	99.78	99.42	98.80	99.81	98.71	98.44	98.96
	Hydrothermal anhydrite														
	QZK401-430										QZK301-142				
CaO	40.31	40.19	39.98	40.30	40.15	39.96	39.51	39.72	39.95	40.17	40.51	40.19	40.07	40.45	40.34
SO_3	59.76	60.17	58.87	58.91	59.56	58.62	59.07	59.75	60.22	59.18	59.46	59.87	59.63	59.72	59.14
P_2O_5	0.03	0.05	0.06	0.07	0.16	0.11	0.05	0.08	0.04	0.02	0.04	0.05	0.00	0.02	0.03
SiO_2	0.04	0.04	0.03	0.03	0.00	0.01	0.02	0.00	0.00	0.01	0.02	0.00	0.02	0.02	0.00
Ce_2O_3	0.00	0.07	0.00	0.06	0.16	0.00	0.05	0.00	0.00	0.07	0.01	0.06	0.00	0.05	0.00
MnO	0.00	0.00	0.01	0.00	0.00	0.00	0.00	0.02	0.00	0.02	0.02	0.02	0.00	0.01	0.00
BaO	0.00	0.00	0.10	0.00	0.03	0.05	0.00	0.00	0.00	0.00	0.00	0.00	0.00	0.04	0.00
SrO	0.10	0.21	0.18	0.15	0.19	0.27	0.34	0.41	0.34	0.34	0.20	0.33	0.22	0.15	0.11
Total	100.24	100.73	99.2	99.52	100.25	99.02	99.04	99.98	100.55	99.81	100.26	100.52	99.94	100.46	99.62
	Apatite within and adjacent to magmatic anhydrite														
	QZK812-472								QZK812-473						
CaO	54.36	54.16	53.86	53.43	53.48	53.96	53.58	53.50	53.64	53.29	53.56	52.90	53.27	53.26	53.01
SO_3	0.13	0.38	0.11	0.17	0.16	0.26	0.14	0.44	0.19	0.27	0.11	0.16	0.13	0.21	0.13
P_2O_5	42.07	42.07	42.63	43.70	43.17	42.25	43.01	43.57	43.91	43.74	44.14	43.75	42.96	43.95	43.44
SiO_2	0.15	0.18	0.15	0.09	0.11	0.19	0.11	0.14	0.18	0.13	0.04	0.15	0.23	0.08	0.13
Ce_2O_3	0.10	0.19	0.09	0.14	0.14	0.18	0.17	0.25	0.18	0.21	0.18	0.20	0.22	0.14	0.20
Y_2O_3	0.00	0.00	0.00	0.00	0.00	0.00	0.00	0.00	0.00	0.00	0.00	0.00	0.00	0.00	0.00
MnO	0.20	0.17	0.19	0.14	0.17	0.10	0.23	0.18	0.19	0.14	0.17	0.21	0.16	0.14	0.20
BaO	0.00	0.00	0.04	0.04	0.00	0.03	0.00	0.00	0.00	0.00	0.11	0.05	0.00	0.00	0.00
SrO	0.00	0.00	0.00	0.00	0.00	0.00	0.00	0.00	0.00	0.00	0.00	0.00	0.00	0.00	0.00
F	3.22	3.12	3.06	3.23	3.14	3.29	3.30	3.25	3.54	3.68	3.39	3.47	3.30	3.22	3.34
Cl	0.30	0.30	0.31	0.17	0.25	0.18	0.35	0.29	0.22	0.09	0.27	0.20	0.31	0.25	0.37
Total	99.11	99.20	99.07	99.72	99.23	99.02	99.41	100.19	100.50	99.99	100.48	99.57	99.12	99.84	99.33

Oxides determined by electron probe microanalysis are reported in weight percent.

a transparent unknown silicate mineral phase, homogenized by disappearance of halite (T_{mNacl}) in B veins.

4. Results

4.1 Anhydrite

The anhydrites and apatites were analyzed by electron probe microanalysis (EPMA) (JEOL JXA-8100 electron microprobe at the Institute of Geology and Geophysics, Chinese Academy of Science [CAS]) with 10 kV beam conditions and 10 nA beam current.

The results (Table 3) show that except strontium, other major (CaO, SO_3) and trace components (P_2O_5, SiO_2, Ce_2O_3 *et al*.) in hydrothermal and magmatic anhydrites are similar. Strontium concentration (SrO) in hydrothermal anhydrite (0.10–0.41 wt%) is higher than that in magmatic anhydrite (0.00–0.11 wt%). Euhedral apatite coexisting within and adjacent to magmatic anhydrite in the unaltered granodiorite has the range of F and Cl concentrations of 3.06–3.68 wt. %, and 0.09–0.37 wt. %, respectively. This composition (F: >1 wt%, F/Cl >1) is typical igneous fluorapatite in granite (Chu *et al*., 2009). The apatites have relative high content of

Ce_2O_3 (0.09–0.25 wt%); sulfur (expressed as SO_3 wt% ranges 0.11–0.44 wt%); and relative low content of MnO (0.1–0.23 wt%). The Sr and Y contents are below detection limit.

4.2 Microthermometry of fluid inclusions

Fluid inclusions in quartz and anhydrite were used for microthermometry study, analyzed on a Linkam THMSG600 gas-flow heating-freezing stage at the Institute of Geology and Geophysics, CAS. The uncertainties of measurements are ± 0.1°C for freezing and ± 1°C for heating. Salinities of fluid inclusions were calculated from the final melting point of ice for two-phase fluid inclusions and halite melting temperature for polyphase fluid inclusions using the equations of Hall *et al*. (1988) and Sterner *et al*. (1988). All the results are shown in Figure 6. Homogenization of all the inclusions takes place at temperatures ranging 196–536°C, rarely >550°C. Most polyphase inclusions have dissolution of halite as the last phase change ($T_{mNacl} > T_f$), which is denoted as halite homogenization (Wilson *et al*., 1980). The dissolution temperature of halite was used for salinity calculation in this study. The salinities are between 2.41 and 60.44 wt% NaCl equivalent. This study did not find any typical CO_2 fluid inclusion.

Quartz phenocrysts in monozogranite porphyry contain all types of fluid inclusions, especially rich in liquid-rich inclusions and polyphase high-salinity inclusions which mostly homogenize by disappearance of halite. Homogenization takes place at temperatures of 384–510°C. Liquid-rich inclusions homogenize at 384–536°C, average 443°C; polyphase high-salinity inclusions homogenize at 414–510°C, average 459°C. The salinity of liquid-rich inclusions and polyphase high-salinity inclusions are between 6.45 and 19.45 wt% NaCl equivalent, average 13.00 wt% NaCl equivalent, and between 49.00 and 59.22 wt% NaCl equivalent, average 54.54 wt% NaCl equivalent, respectively. Vapor-rich inclusions homogenize at temperatures of 426–505°C, average 473°C; the salinity of these are between 4.10 and 9.80 wt% NaCl equivalent, average 5.97 wt% NaCl equivalent (Fig. 6a, b).

Table 4 shows the results of the homogenization temperatures and salinity of fluid inclusions in quartz in the phenocrysts and each vein type. A vein contains all types of fluid inclusions, especially rich in vapor-rich inclusions and polyphase high-salinity inclusions which mostly homogenize by disappearance of halite. B vein contains all types of fluid inclusions except vapor-rich fluid inclusions; the polyphase high-salinity inclusions mostly homogenize by disappearance of vapor or halite and vapor disappearance over a small temperature interval. D vein contains a few fluid inclusions, commonly with liquid-rich inclusions and polyphase high-salinity inclusions which homogenize by disappearance of vapor. Both the homogenization temperature and salinity are lower than A and B veins (Fig. 6).

Compared to quartz, anhydrite in A veins and breccia, only contain two-phase inclusions (Fig. 5f) (mostly type 1, rarely type 2). It is difficult to observe the process of freezing of fluid in anhydrite, because of their cubic negative-crystal shapes and dark cavity walls. Therefore, this study lacks any salinity data of fluid inclusions in anhydrite. In A veins, fluid inclusions in anhydrites homogenize at temperatures of 260–393°C, average 339°C. This range is distinctly lower than those of the coexisting quartz, which range from 346°C to 405°C (average 370°C) (Fig. 7a). This result is consistent with the observation that anhydrite usually occurs interstitially between quartz crystals.

Polyphase fluid inclusions homogenized by halite dissolution are ubiquitous in the Qulong porphyry deposit, which is commonly observed in porphyry copper and similar magmatic-hydrothermal ore deposits (Becker *et al*., 2008). Polyphase fluid inclusions homogenized in three different ways ($T_{mNaCl} < T_f$, $T_{mNaCl} = T_f$, $T_{mNaCl} > T_f$), suggesting that pressure varied during mineralization (Li & Sasaki, 2007; Becker *et al*., 2008). In this paper, we assume fluid boiling and calculate trapping pressure of the fluid in the Qulong deposit (Fig. 8) as 35–60 Mpa at 460–510°C in quartz phenocrysts and 28–42 Mpa at 400–450°C in A veins.

5. Discussion and conclusions

Formation of giant porphyry copper deposits requires either highly efficient collection of Cu from large volumes of magma (Cline & Bodnar, 1991; Cloos, 2001), unusually Cu-rich parental magmas (Core *et al*., 2006), and/or an anomalously S-rich source (Halter *et al*., 2005). In giant porphyry deposits, the amount of sulfur is too large to be supplied from a small volume of immediate host rocks; sulfur was likely supplied from magmatic anhydrite (Hattori & Keith, 2001; Chambefort *et al*., 2008). At the Qulong porphyry Cu–Mo deposit, we confirmed the presence of magmatic anhydrite and hydrothermal anhydrite, which is evidence of a highly oxidized magmatic-hydrothermal condition.

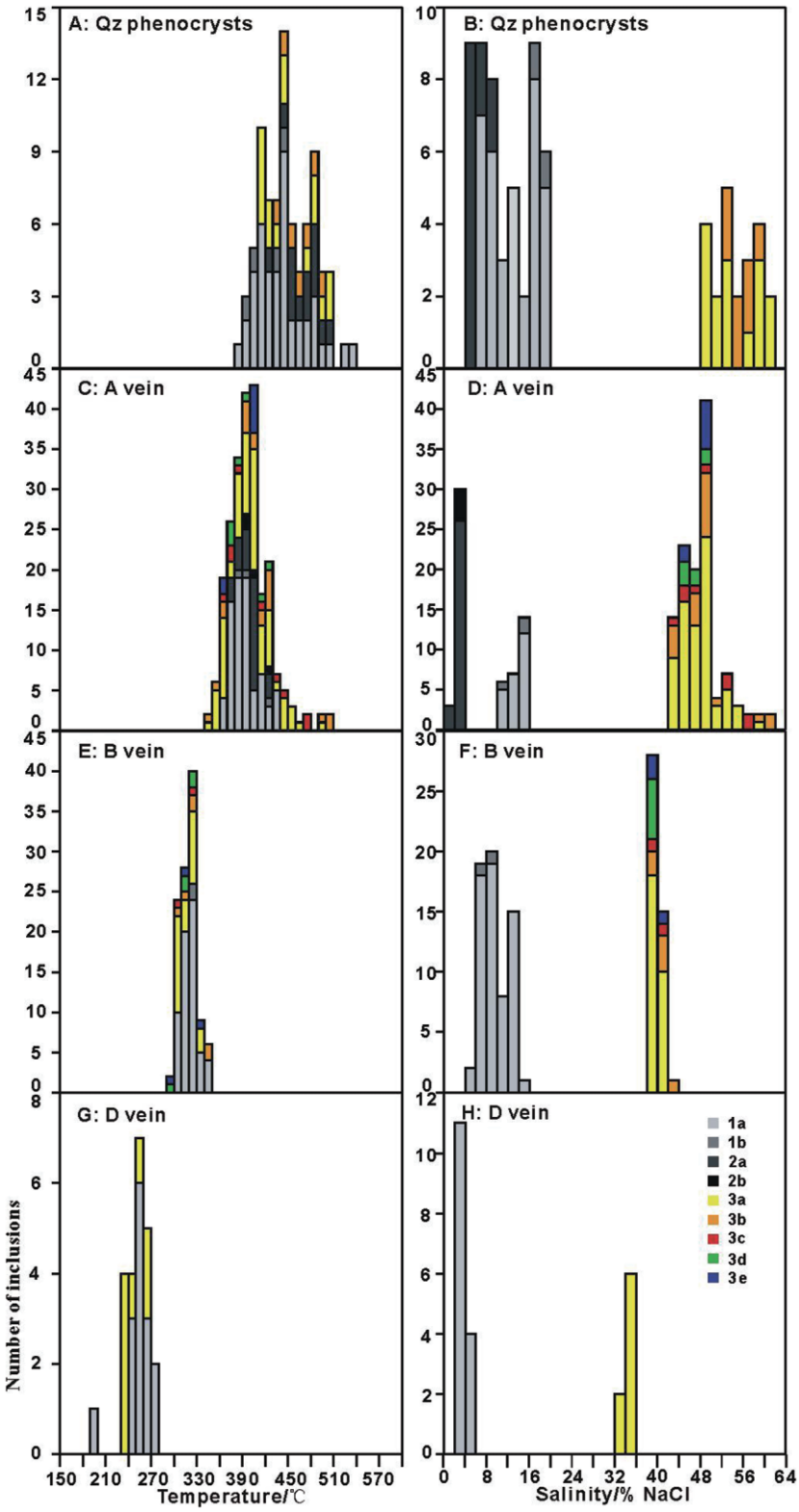

Fig. 6 Salinity versus final homogenization temperature (to liquid or by halite melting) for all inclusions of the Qulong porphyry Cu–Mo deposit.

Table 4 Final homogenization temperature and salinity for all inclusions in different veins of the Qulong porphyry Cu–Mo deposit

	Types	Tm (°C)	Salinity (% NaCl equivalent)
Quartz phenocrysts	1a,b	384–536, av. 443	6.45–19.45, av. 13.00
	2a	426–505, av. 473	4.10–9.80, av. 5.97
	3a,b	414–510, av. 459	49.00–59.22, av. 54.54
A veins	1a,b	369–439, av. 394	10.73–15.86, av.13.47
	2a,b	375–425, av. 402	1.90–2.80, av. 2.43
	3a,b,c,e	350–505, av. 405	42.40–60.44, av. 48.13
B veins	1a,b	302–344, av. 322	5.71–14.97, av. 10.00
	3a,b,c,d,e	298–346, av. 318	38.01–42.03, av. 39.66
D veins	1a	196–273, av. 254	2.41–5.86, av. 3.71
	3a	238–270, av. 249	33.95–35.99, av. 34.65

The sulfur speciation and solution mechanisms in silicate melts is controlled by the pressure, temperature, melt composition and oxidation state; under oxidizing conditions sulfur is dissolved mainly as S^{6+} (>90% of total sulfur) and sulfur solubility in oxidized magmas is quite higher than in reduced conditions (Carroll & Rutherford, 1985, 1987, 1988; Luhr, 1990; Nilsson & Peach, 1993; Wallace & Carmichael, 1994; Fleet *et al*., 2005; Jugo *et al*., 2005; Wilke *et al*., 2008; Jugo, 2009). The anhydrite-bearing rock eruptions of El Chichón volcano in 1982 (Luhr *et al*., 1984) and Mount Pinatubo in 1990 (Bernard *et al*., 1991) demonstrated that sulfate species (SO_4^{2-}) are significant in some magmatic systems. Magmas which contain magmatic anhydrite are also known to be water-rich (Luhr, 2008). The oxidized and high water content intermediate to felsic igneous rocks are common in island arc environments, and have potential to form mineral deposits (Ishihara, 1981; Becker & Rutherford, 1996), especially for porphyry Cu-(Au) type deposits (Imai *et al*., 1993; De Hoog *et al*., 2004; Li *et al*., 2006b, 2007b; Luhr, 2008; Sillitoe, 2010).

In this study, we confirm a highly oxidized, sulfur-rich magma-hydrothermal system in the Gangdese orogenic setting, which is assumed to be a non-subduction setting. The oxidized magma can effectively scavenge sulfur from sulfides in the source region (De Hoog *et al*., 2004); thus, it could deliver sulfur into the shallow crust during the magma ascent and consequently form a productive porphyry system at the orogenic setting just as at the subduction setting.

At Qulong, apatite is included in or clustered with anhydrite, as at El Chichon (Luhr *et al*., 1984). In apatite, sulfur dissolved as the sulfate molecule in its crystalline structure principally by the substitution $S^{6+}+Si^{4+} = 2P^{5+}$ or $S^{6+}+Na^{+} = P^{5+}+Ca^{2+}$ (Streck & Dilles, 1998). The high S abundances in apatite (0.11–0.44 wt%, expressed as SO_3 wt. %) at Qulong is related to the oxidized condition of the host magma. Usually, the sulfur (SO_3) contents of apatite in porphyry ore-related igneous rocks (>0.10 wt%) are higher than that in barren igneous rocks (<0.10 wt%) (Imai, 2002, 2004) and are also considered to reflect the redox state of the magma source region or fluids encountered during magma generation (Imai, 2004). The sulfur concentration in apatite (0.11–0.44 wt% SO_3) at Qulong is higher than that (0.00–0.30 wt% SO_3) in the Dexing porphyry Cu deposit, Jiangxi Province, southeast China (Yao *et al*., 2007).

In conclusion, as described above, from quartz phenocrysts in porphyry to A, B and D veins, the final homogenization temperatures of all type inclusions decreased from about 450°C to 250°C (Fig. 6 and Table 4) and the salinities decreased from about 54 wt% NaCl equivalent to 34 wt% NaCl equivalent. Based on the crosscutting relations and the mineralization features between different veins, the changes of temperature and salinity may account for mineralization at the Qulong deposit: sulfide precipitation resulted from the cooling magmatic-hydrothermal fluid system and abundant copper-bearing sulfides were deposited during the formation of A and B veins at about 320–400°C. Fluid boiling assumed from the fluid inclusions in quartz phenocysts and A veins may suggest the depths of fluid trapping at approximately 1.4–2.4 km and 1.1–1.7 km, respectively (Fig. 8).

Acknowledgments

This research was supported by the NSFC (Grant no. 40772066), the National Eleventh-Five years project (Grant no. 2006BA01A04) and Chinese Geological Survey research project (Grant no. 20089932). The authors would like to extend their gratitude to Dr. Qian

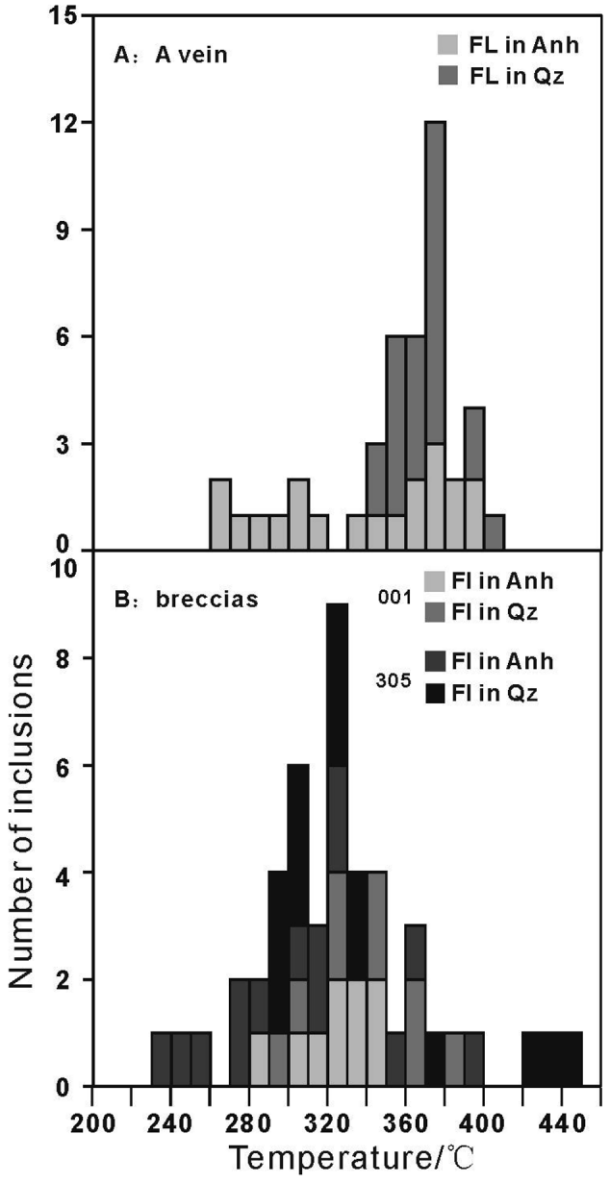

Fig. 7 Final homogenization temperature of fluid inclusions in anhydrite (An) and quartz (Qz) in A veins and breccia of the Qulong porphyry Cu–Mo deposit.

Mao and Mr. Yugang Ma for their assistance in EPMA analyses. We would like to express our gratitude to Prof. Zengqian Hou and the geologists from the Tibet Julong Copper Co., Ltd. for their kindly help and valuable discussions. And thanks Dr. A. J. Wilson for improving the English. We are very grateful to two reviewers for their constructive criticism and valuable comments on the manuscript.

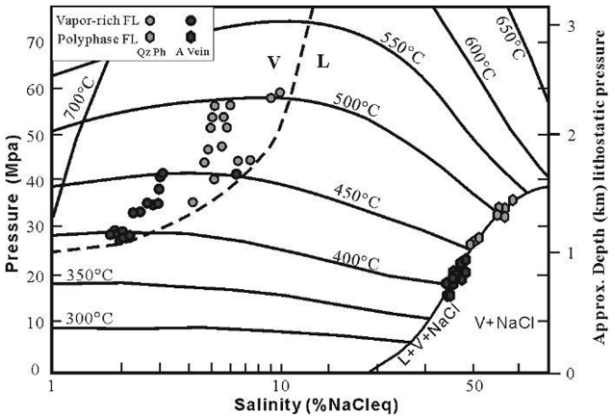

Fig. 8 Pressure estimates for boiling fluid inclusions assemblage from the Qulong porphyry Cu–Mo deposit (Original plot after Bouzari & Clark, 2006).

References

Aitchison, J. C., Ali, J. R. and Davis, A. M. (2007) When and where did India and Asia collide. J. Geophys. Res., 112, B05423. doi: 10.1029/2006JB004706.

Allègre, C. J., Courtillot, V., Tapponnier, P., Hirn, A., Mattauer, M., Coulon, C., Jaeger, J. J., Achache, J., Schärer, U., Marcoux, J., Burg, J. P., Girardeau, J., Armijo, R., Gariépy, C., Göpel, C., Li, T. D., Xiao, X. C., Chang, C. F., Li, G. Q., Lin, B. Y., Teng, J. W., Wang, N. W., Chen, G. M., Han, T. L., Wang, X. B., Deng, W. M., Sheng, H. B., Cao, Y. G., Zhou, J., Qiu, H. R., Bao, P. S., Wang, S. C., Wang, B. X., Zhou, Y. X. and Xu, R. H. (1984) Structure and evolution of the Himalayan-Tibet orogenic belt. Nature, 307, 17–22.

Baker, L. L. and Rutherford, M. J. (1996) Crystallisation of anhydrite-bearing magmas, Special Paper 315: The Third Hutton Symposium on the Origin of Granites and Related Rocks, 243–250.

Becker, S. P., Fall, A. and Bodnar, R. J. (2008) Synthetic fluid inclusions. XVII. PVTX properties of high salinity H_2O-NaCl solutions (>30 wt% NaCl): Application to fluid inclusions that homogenize by halite disappearance from porphyry copper and other hydrothermal ore deposits. Econ. Geol., 103, 539–554.

Bernard, A., Demaiffe, D., Mattielli, N. and Punongbayan, R. S. (1991) Anhydrite-bearing pumices from Mount Pinatubo: Further evidence for the existence of sulfur-rich silicic magmas. Nature, 354, 139–140.

Blevin, P. L. and Chappell, B. W. (1992) The role of magma sources, oxidation states and fractionation in determining the granite metallogeny of eastern Australia. Trans. R. Soc. Edinb. Earth Sci., 83, 305–316.

Bouzari, F. and Clark, A. H. (2006) Prograde evolution and geothermal affinities of a major porphyry copper deposit: The Cerro Colorado hypogene protore, I Región, Northern Chile. Econ. Geol., 101, 95–134.

Burnham, C. W. and Ohmoto, H. (1980) Late-stage processes of felsic magmatism. In Ishihara, S. and Takenouchi, S. (eds.) Granitic Magmatism and Related Mineralization. Mining Geology Special Issue. Soc. Res. Geol, Tokyo, 1–13.

Carroll, M. R. and Rutherford, M. J. (1985) Sulfide and sulfate saturation in hydrous silicate melts. J. Geophys. Res., 90, 601–612.

Carroll, M. R. and Rutherford, M. J. (1987) The stability of igneous anhydrite: experimental results and implications for sulfur behavior in the 1982 El Chichón trachyandesite and other evolved magmas. J. Petrol., 28, 781–801.

Carroll, M. R. and Rutherford, M. J. (1988) Sulfur speciation in hydrous experimental glasses of varying oxidation state: Results from measured wavelength shifts of sulfur X-rays. Am. Min., 73, 845–849.

Chambefort, I., Dilles, J. H. and Kent, A. J. R. (2008) Anhydrite-bearing andesite and dacite as a source for sulfur in magmatic-hydrothermal mineral deposits. Geology, 36 (9), 719–722.

Chu, M. F., Wang, K. L., Griffin, W. L., Chung, S. L., O'Reilly, S. Y., Pearson, N. J. and Iizuka, Y. (2009) Apatite composition: Tracing petrogenetic processes in Transhimalayan granitoids. J. Petrol., 50, 1829–1855.

Cline, J. S. and Bodnar, R. J. (1991) Can economic porphyry mineralization be generated by a typical calc-alkaline melt? J. Geophy. Res., 96, 8113–8126.

Cloos, M. (2001) Bubbling magma chambers, cupolas, and porphyry copper deposits. Inter. Geo. Rev., 43, 285–311.

Coleman, M. and Hodges, K. (1995) Evidence for Tibetan Plateau uplift before 14 Ma ago from a new minimum age for east-west extension. Nature, 374, 49–52.

Core, D. P., Kesler, S. E. and Essene, E. J. (2006) Unusually Cu-rich magmas associated with giant porphyry copper deposits: Evidence from Bingham, Utah. Geology, 34, 41–44.

Coulon, C., Maluski, H., Bollinger, C. and Wang, S. (1986) Mesozoic and Cenozoic volcanic rocks from central and southern Tibet: $^{39}Ar/^{40}Ar$ dating, petrological characteristics and geodynamical significance. Earth Planet. Sci. Lett., 79, 281–302.

De Hoog, J. C. M., Hattori, K. H. and Hoblitt, R. P. (2004) Oxidized sulfur-rich mafic magma at Mount Pinatubo, Philippines. Contrib. Mineral. Petrol., 146, 750–761.

Defant, M. J. and Drummond, M. S. (1990) Derivation of some modern arc magmas by melting of young subducted lithosphere. Nature, 347, 662–665.

Dilles, J. H. and Einaudi, M. T. (1992) Wall-rock alteration and hydrothermal flow paths about the Ann-Mason porphyry copper deposit, Nevada: A 6-km vertical reconstruction. Econ. Geol., 87, 1963–2001.

Dong, Y. H., Xu, J. F., Zeng, Q. G., Mao, G. Z. and Li, J. (2006) Is there a Neo-Tethys' subduction record earlier than arc volcanic rocks in the Sangri group? Acta Petrologica Sinica, 22, 661–668. (in Chinese with English Abstract).

Fleet, M. E., Liu, X., Harmer, S. L. and King, P. L. (2005) Sulfur K-edge XANES spectroscopy: Chemical state and content of sulfur in silicate glasses. Cana. Min, 43, 1605–1618.

Geng, Q. R., Pan, G. T., Wang, L. Q., Zhu, D. C. and Liao, Z. L. (2006) Isotopic geochronology of the volcanic rocks from the Yeba Formation in the Gangdise zone, Xizang. Sedimentary Geology and Tethyan Geology, 26, 1–7. (in Chinese with English Abstract).

Gustafson, L. B. and Hunt, J. P. (1975) The porphyry copper deposit at El Salvador, Chile. Econ. Geol., 70, 857–912.

Hall, D. L., Sterner, S. M. and Bodnar, R. J. (1988) Freezing point depression of NaCl-KCl-H_2O solutions. Econ. Geol., 83 (1), 197–202.

Halter, W. E., Heinrich, C. A. and Pettke, T. (2005) Magma evolution and the formation of porphyry Cu-Au ore fluids: Evidence from silicate and sulfide melt inclusions. Miner. Deposita, 39, 845–863.

Harrison, T. M., Copeland, P., Kidd, W. S. F. and Lovera, O. M. (1995) Activation of the Nyainqentanghla shear zone: Implications for uplift of the southern Tibetan Plateau. Tectonics, 14, 658–676.

Harrison, T. M., Copeland, P., Kidd, W. S. F. and Yin, A. (1992) Raising Tibet. Science, 255, 1663–1670.

Hattori, K. and Keith, J. D. (2001) Contribution of mafic melt to porphyry copper mineralization: Evidence from Mount Pinatubo, Philippines, and Bingham Canyon, Utah, USA. Miner. Deposita, 26, 799–806.

Hou, Z. Q., Pan, G. T., Wang, A. J., Mo, X. X., Tian, S. H., Sin, X. M., Ding, L., Wang, E. Q., Gao, Y. F., Xie, Y. L., Zeng, P. S., Qin, K. Z., Xu, J. F., Qu, X. M., Yang, Z. M., Yang, Z. S., Fei, H. C. and Li, Z. Q. (2006b) Metallogenesis in Tibetan collisional orogenic belt: Mineralization in late-collisional transformation setting. Mineral Deposits, 25, 521–542. (in Chinese with English abstract).

Hou, Z. Q., Qu, X. M., Yang, Z. S., Meng, X. J., Li, Z. Q., Yang, Z. M., Zheng, M. P., Zheng, Y. Y., Nie, F. J., Gao, Y. F., Jiang, S. H. and Li, G. M. (2006c) Metallogenesis in Tibetan collisional orogenic belt: Mineralization in post-collisional extension setting. Mineral Deposits, 25, 629–651. (in Chinese with English abstract).

Hou, Z. Q., Yang, Z. M., Qu, X. M., Meng, X. J., Li, Z. Q., Beaudoin, G., Rui, Z. Y., Gao, Y. F. and Zaw, K. (2009) The Miocene Gangdese porphyry copper belt generated during post-collisional extension in the Tibetan Orogen. Ore Geol. Rev., 36, 25–51.

Hou, Z. Q., Yang, Z. S., Xu, W. Y., Mo, X. X., Ding, L., Gao, Y. F., Dong, F. L., Li, G. M., Qu, X. M., Li, G. M., Zhao, Z. D., Jiang, S. H., Meng, X. J., Li, Z. Q., Qin, K. Z. and Yang, Z. M. (2006a) Metallogenesis in Tibetan collisional orogenic belt: ? Mineralization in main-collisional orogenic setting. Mineral Deposits, 25, 337–458. (in Chinese with English abstract).

Imai, A. (2002) Metallogenesis of porphyry Cu deposits of the western Luzon arc, Philippines: K-Ar ages, SO_3 contents of microphenocrystic apatite and significance of intrusive rocks. Resour. Geol., 52, 147–161.

Imai, A. (2004) Variation of Cl and SO_3 contents of microphenocrystic apatite in intermediate to silicic igneous rocks of Cenozoic Japanese island arcs: Implications for porphyry Cu metallogenesis in the Western Pacific island arcs. Resour. Geol., 54, 357–372.

Imai, A., Listanco, E. L. and Fujii, T. (1993) Petrologic and sulfur isotopic significance of highly oxidized and sulfur-rich magma of Mt. Pinatubo, Philippines. Geology, 21, 699–702.

Ishihara, S. (1977) The magnetite series and ilmenite-series granitic rocks. Min. Geol., 27, 293–305.

Ishihara, S. (1981) The granitoid series and mineralization: Economic geology 75th anniversary volume. Soc. Econ. Geol, 75, 458–484.

Jugo, P. J. (2009) Sulfur content at sulfide saturation in oxidized magmas. Geology, 37, 415–418.

Jugo, P. J., Luth, R. and Richards, J. P. (2005) An experimental study of the sulfur content in basaltic melts saturated with immiscible sulfide or sulfate liquids at 1300? and 1.0 GPa. J. Petrol., 46, 783–798.

Keith, S. B. and Swan, M. M. (1995) The great Laramide porphyry copper cluster of Arizona, Sonora, and New Mexico: The tectonic setting, petrology, and genesis of a world-class porphyry metal cluster. In Coyner, A. R. and Fahey, P. L. (eds.) Geology and Ore Deposits of the American Cordillera. Geological Society of Nevada, Reno, NV, 1667–1747.

Li, G. M., Li, J. X., Qin, K. Z., Zhang, T. P. and Xiao, B. (2007a) High temperature, salinity and strong oxidation ore-forming fluid at Duobuza gold-rich porphyry copper deposit in the Bangonghu tectonic belt, Tibet: Evidence from fluid inclusions. Acta Petrologica Sinica, 23, 935–952. (in Chinese with English abstract).

Li, G. M., Qin, K. Z., Ding, K. S., Liu, T. B., Li, J. X., Wang, S. H., Jiang, S. Y. and Zhang, X. C. (2006a) Geology, Ar-Ar age and mineral assemblage of Eocene skarn Cu-Au±Mo deposits in the Southeastern Gangdese arc, Southern Tibet: Implications for deep exploration. Resour. Geol., 56, 197–217.

Li, J. X., Qin, K. Z. and Li, G. M. (2006b) Basic characteristics of gold-rich porphyry copper deposits and their ore sources and evolving processes of high oxidation magma and ore-forming fluid. Acta Petrologica Sinica, 22, 678–688. (in Chinese with English abstract).

Li, J. X., Qin, K. Z., Li, G. M. and Yang, L. K. (2007b) K-Ar and $^{40}Ar/^{39}Ar$ age dating of Nimu porphyry copper orefield in Central Gangdese: Constrains on magmatic-hydrothermal evolution and ore-forming tectonic setting. Acta Petrologica Sinica, 23, 953–966. (in Chinese with English abstract).

Li, X. F. and Sasaki, M. (2007) Hydrothermal Alteration and Mineralization of Middle Jurassic Dexing Porphyry Cu-Mo Deposit, Southeast China. Resour. Geol., 57, 409–426.

Luhr, J. F. (1990) Experimental phase relations of water-saturated and sulfur-saturated arc magmas and the 1982 eruptions of El Chichón volcano. J. Petrol., 31, 1071–1114.

Luhr, J. F. (2008) Primary igneous anhydrite: Progress since its recognition in the 1982 El Chichón trachyandesite. J. Volcanol. Geotherm. Res., 175, 394–407.

Luhr, J. F., Carmichael, I. S. E. and Varekamp, J. C. (1984) The 1982 eruptions of El Chichón volcano, Chiapas, Mexico: Mineralogy and petrology of the anhydrite phenocryst-bearing pumices. J. Volcanol. Geotherm. Res., 23, 69–108.

Mo, X. X., Hou, Z. Q., Niu, Y. L., Dong, G. C., Qu, X. M., Zhao, Z. D. and Yang, Z. M. (2007) Mantle contributions to crustal thickening during continental collision: Evidence from Cenozoic igneous rocks in southern. Tibet. Lithos, 96, 225–242.

Mo, X. X., Niu, Y. L., Dong, G. C., Zhao, Z. D., Hou, Z. Q., Zhou, S. and Ke, S. (2008) Contribution of syncollisional felsic magmatism to continental crust growth: A case study of the Paleogene Linzizong volcanic Succession in southern Tibet. Chem. Geol., 250, 49–67.

Nilsson, K. and Peach, C. L. (1993) Sulfur speciation, oxidation state, and sulfur concentration in backarc magmas. Geochim. Cosmochim. Acta, 57, 3807–3813.

Qin, K. Z., Li, G. M., Zhao, J. X., Li, J. X., Xue, G. Q., Yan, G., Su, D. K., Xiao, B., Chen, L. and Fan, X. (2008) Discovery of Sharang large-scale porphyry molybdenum deposit, the first single Mo deposit in Tibet and its significance. Geology in China, 35, 1101–1112. (in Chinese with English abstract).

Qin, K. Z., Tosdal, R., Li, G. M., Zhang, Q. and Li, J. L. (2005) Formation of the Miocene porphyry Cu (-Mo-Au) deposits in the Gangdese arc, southern Tibet, in a transitional tectonic setting. In Zhao, C. C. and Guo, B. J. (eds.) Mineral Deposit Research: Meeting the Global Challenge., Vol. 3. China Land Publishing House, Beijing, 44–47.

Qu, X. M., Hou, Z. Q. and Li, Y. G. (2004) Melt components derived from a subducted slab in late orogenic ore-bearing porphyries in the Gangdese copper belt, southern Tibetan Plateau. Lithos, 74, 131–148.

Roedder, E. (1984) Fluid inclusions. Reviews in Mineralogy, vol. 12. Mineralogical Society of America, VA, USA.

Rui, Z. Y., Hou, Z. Q., Qu, X. M., Zhang, L. S., Wang, L. S. and Liu, Y. L. (2003) Metallogenetic epoch of Gangdese Porphyry Copper Belt and uplift of Qinghai-Tibet Plateau. Mineral Deposits, 22, 217–225. (in Chinese with English abstract).

Sillitoe, R. H. (2010) Porphyry copper systems. Econo. Geol., 105, 3–41.

Sterner, S. M., Hall, D. L. and Bodnar, R. J. (1988) Synthetic fluid inclusions. V. Solubility relations in the system NaCl-KCl-H_2O under vapor-saturated conditions. Geochim. Cosmochim. Acta, 52, 989–1006.

Streck, M. J. and Dilles, J. H. (1998) Sulfur evolution of oxidized arc magmas as recorded in apatite from a porphyry copper batholith. Geology, 26, 523–526.

Tibet Julong Copper Co., Ltd. (2008) Qulong copper polymetallic deposit exploration report. Maizhokunggar County, Tibet.

Wallace, P. J. and Carmichael, I. S. E. (1994) S speciation in submarine basaltic glasses as determined by measurement of SKa X-ray wavelength shifts. Am. Min., 79, 161–167.

Wang, L. L., Mo, X. X., Li, B., Dong, G. C. and Zhao, Z. D. (2006) Geochronology and geochemistry of the ore-bearing porphyry in Qulong Cu (Mo) ore deposit, Tibet. Acta Petrologica Sinica, 22, 1001–1008. (in Chinese with English abstract).

Wilke, M., Jugo, P. J., Klimm, K., Susini, J., Botcharnikov, R., Kohn, S. C. and Janousch, M. (2008) The origin of S^{4+} detected in silicate glasses by XANES. Am. Min., 93, 235–240.

Williams, H., Turner, S., Kelly, S. and Harris, N. (2001) Age and composition of dikes in southern Tibet: New constraints on the timing of east-west extension and its relationship to post-collisional volcanism. Geology, 29, 339–342.

Wilson, J. W. J., Kesler, S. E., Cloke, P. L. and Kelley, W. C. (1980) Fluid inclusion geochemistry of the Granisle and Bell porphyry copper deposits, British Columbia. Econ. Geol., 75, 45–61.

Xiao, B., Qin, K. Z., Li, G. M., Li, J. X., Xia, D. X., Chen, L. and Zhao, J. X. (2009) S-rich, highly-oxidized ore-bearing magma in the Qulong giant porphyry-type Cu-Mo deposit in southern. Tibet. Acta Geologica Sinica, 83, 1860–1868. (in Chinese with English Abstract).

Yang, Z. M., Hou, Z. Q., White, N. C., Chang, Z. S., Li, Z. Q. and Song, Y. C. (2009) Geology of the post-collisional porphyry copper-molybdenum deposit at Qulong, Tibet. Ore Geol. Rev., 36, 133–159.

Yao, C. L., Lu, J. J. and Guo, W. M. (2007) Compsitional difference between three generations of apatite from Tongchang porphyry copper deposit, Jiangxi Province, Southeast China. Acta Mineralogica Sinica, 27, 31–40. (in Chinese with English abstract).

Yin, A. and Harrison, T. M. (2000) Geologic evolution of the Himalayan-Tibetan orogen. Annu. Rev. Earth Planet. Sci., 28, 211–280.